

Robust segmentation methods with an application to aortic pulse wave velocity calculation



Danilo Babin ^{a,*}, Daniel Devos ^{b,1}, Aleksandra Pižurica ^{a,2}, Jos Westenberg ^c, Ewout Vansteenkiste ^{a,3}, Wilfried Philips ^{a,4}

^a Department of Telecommunications and Information Processing – TELIN-IPI-iMinds, Faculty of Sciences, Ghent University, Sint-Pietersnieuwstraat 41, B-9000 Ghent, Belgium

^b Department of Radiology, Cardiovascular MR & CT, Ghent University Hospital, De Pintelaan 185, B-9000 Ghent, Belgium

^c Department of Radiology, LUMC, Leiden University Medical Center, Albinusdreef 2, 2333 ZA Leiden, The Netherlands

ARTICLE INFO

Article history:

Received 5 April 2013

Received in revised form 6 November 2013

Accepted 9 December 2013

Keywords:

Image segmentation

Multiscale segmentation

Pulse wave velocity

ABSTRACT

Aortic stiffness has proven to be an important diagnostic and prognostic factor of many cardiovascular diseases, as well as an estimate of overall cardiovascular health. Pulse wave velocity (PWV) represents a good measure of the aortic stiffness, while the aortic distensibility is used as an aortic elasticity index. Obtaining the PWV and the aortic distensibility from magnetic resonance imaging (MRI) data requires diverse segmentation tasks, namely the extraction of the aortic center line and the segmentation of aortic regions, combined with signal processing methods for the analysis of the pulse wave. In our study non-contrasted MRI images of abdomen were used in healthy volunteers (22 data sets) for the sake of non-invasive analysis and contrasted magnetic resonance (MR) images were used for the aortic examination of Marfan syndrome patients (8 data sets). In this research we present a novel robust segmentation technique for the PWV and aortic distensibility calculation as a complete image processing toolbox. We introduce a novel graph-based method for the centerline extraction of a thoraco-abdominal aorta for the length calculation from 3-D MRI data, robust to artifacts and noise. Moreover, we design a new projection-based segmentation method for transverse aortic region delineation in cardiac magnetic resonance (CMR) images which is robust to high presence of artifacts. Finally, we propose a novel method for analysis of velocity curves in order to obtain pulse wave propagation times. In order to validate the proposed method we compare the obtained results with manually determined aortic centerlines and a region segmentation by an expert, while the results of the PWV measurement were compared to a validated software (LUMC, Leiden, the Netherlands). The obtained results show high correctness and effectiveness of our method for the aortic PWV and distensibility calculation.

© 2013 Elsevier Ltd. All rights reserved.

1. Introduction

Aortic stiffness is an important factor in estimating the cardiovascular risk in several disease conditions. The pulse wave velocity (PWV) is a good indicator of the aortic stiffness in patients with hypertension [1], Marfan syndrome [2,3], metabolic syndrome [4], Diabetes [5], etc. The PWV is a cardiovascular parameter which

is intensively studied [6] both in humans and animals [7]. Aortic PWV is a strong predictor of cardiovascular events and all-cause mortality [8]. The PWV is measured using various techniques [9,10]. The main idea behind the PWV calculation is to track the propagation of the pulse wave from the ascending level of the aorta to its abdominal level in order to obtain the transition speed.

We classify approaches for the PWV measurement into three categories: the blood pressure, ultrasound Doppler and magnetic resonance (MR) techniques. The blood pressure PWV analysis is done using a cuff sphygmomanometer on a peripheral limb, where the measured values reflect the pressure throughout the arterial tree in large conduit arteries. The commercially available hardware (TensioClinic Arteriograph) [11] uses the time interval between the pulse wave (the early systolic peak) and its reflection from the abdominal aortic bifurcation (the late systolic peak). However, the PWV values are obtained using an estimate of the aortic

* Corresponding author. Tel.: +32 92644226.

E-mail addresses: dbabin@telin.ugent.be (D. Babin), daniel.devos@ugent.be (D. Devos), sanja@telin.ugent.be (A. Pižurica), jj.m.westenberg@lumc.nl (J. Westenberg), ervsteen@telin.ugent.be (E. Vansteenkiste), philips@telin.ugent.be (W. Philips).

¹ Tel.: +32 486535312.

² Tel.: +32 92643415.

³ Tel.: +32 498769643.

⁴ Tel.: +32 92643385.

length between the jugulum and the symphysis, which introduces inaccuracies in measurements. The pulsed wave (PW) ultrasound Doppler hardware (e.g. Siemens, Philips) uses the Doppler effect to determine the transition time of the pulse wave in the aorta. However, the length of the aorta still needs to be estimated, resulting in a lower accuracy of the PWV measures. The same approach is taken if a heart sound sensor is used.

Various approaches exist to PWV calculation using MR images. The transit time (TT) approach requires modulus and phase-contrast images at various aortic levels to calculate the velocity curves and a whole MR abdomen and thorax image to calculate aortic lengths between the given levels. The PWV is calculated as the speed of wave propagation. Often only two cross-sectional slices are required for calculating the velocity wave profiles, where the aortic length is measured from an oblique sagittal slice. The time interval between pulse wave is often determined by the “foot” of the wave curve [12]. Algorithms based on finding the maximum (or the minimum) velocity of the pulse wave depend on the assumption that the sampling rate at which the images were taken is sufficiently high to accurately capture the peak of the wave. Similar approach is to define the wave arrival moment as the time instant in which the wave reaches its mid-range value (the average of the minimum and the maximum value). The flow area (QA) approach [13] uses one data set at one site across the aorta (cross-sectional through-plane velocity encoding), where the aortic area is acquired from magnitude images and the flow from phase-contrast images. The PWV is estimated as the ratio of difference in the total (the maximum and the minimum) flow and difference in the total area at early systole. The extension to TT approach is a *multisite method* that uses a single para-sagittal slice of aorta, which allows for obtaining flow waveforms at multiple locations along the aorta. The multi-site method [14] uses the maximum velocity change (at a single cross section) to define the arrival moment of the pulse (at the given cross section). The cross-correlation (XC) approach [15] is a multisite method that uses cross-correlation to determine the time interval between flow waves at different locations along the aorta. A flow-sensitive 4D MRI approach for PWV measurements has also been proposed [16]. An axial velocity profile method for estimating the PWV of the descending aorta was developed in [17], which allows visualization of the pulse wave propagation. Apart from these, methods based on deformable surfaces are applied to the segmentation of modulus images for an aortic distensibility calculation [18]. The comparison of MR PWV calculation approaches was done in [9] and concluded that TT and XC methods result in a closer and a more reproducible aortic PWV measurement than in the QA method.

The current reviews on vessel extraction techniques [19,20] show a wide variety of segmentation methods developed for angiographic vessel images using level-sets [21], machine learning [22], edge detection [23], etc. “Black-blood” vessel extraction methods show good results on segmenting the vessel wall, usually with some user interaction needed: [24] uses discrete dynamic contours, [25] uses deformable models with the Markov Random Fields and a multiscale method is used in [26], robust enough to deal with slice discontinuities and blood flow artifacts. However, the method is not computationally efficient (it needs 8 min on average to segment a single MRI data set). The method of [27] (MiaLite application) is optimized for the segmentation of the abdominal aorta and uses a modified sparse field level set method, with a periodic monotonic speed function, resulting in coherent propagation of the contour boundary. The ITK-SNAP application [28] implements two well-known 3-D active contour segmentation methods: Geodesic Active Contours [29] and Region Competition [30]. The method of [31] (implemented in 3D Slicer) uses seed points to extract the local robust statistics to describe the object features. It evolves several active contours simultaneously with their interactions being

motivated by the principles of action and reaction converging to equilibrium.

The main idea in our work is to design a complete PWV analysis software tool for subjects scanned without injection of contrast agent (for aorta check-up purposes), as well as for patients (studied with contrast images) [32]. First, we propose a novel method for extracting the centerline of the abdominal aorta in contrasted and black-blood MR images by combining graphs and our previous work on multiscale profiling [33]. Next, we introduce a method for the segmentation of the aortic region in modulus images by selection of candidate regions obtained using projections [34]. Finally, we propose a novel method for the analysis of the pulse wave by taking into account its steepest slopes and deformation over time. In order to validate our algorithm, we compare our results to the results of already validated method for pulse wave analysis using the FLOW package for analysis of phase-contrast images and an in-house developed PWV tool [35–37] (LUMC, Leiden, the Netherlands).

2. Materials and methods

2.1. Problem definition and data sets

Data sets for the PWV calculation consist of a 3-D MRI image (as a series of 2-D slices) of an abdomen and thorax and series of modulus and phase-contrast images at different aortic levels represented as time series of 2-D slices. The number of aortic levels at which the Cine series are recorded is arbitrary (unlimited). In this paper, we use four different aortic positions: ascending, descending, diaphragmal and abdominal levels (see Fig. 1). The main idea of our research is to develop an image processing toolkit for the PWV calculation for contrast enhanced or non-contrast enhanced MRI images. Hence, the experiments are conducted on images of healthy volunteers (22 data sets) and Marfan syndrome patients (8 data sets) obtained from the Ghent University Hospital (UZ Gent). We will now describe the used Cine imaging and, in succession, structural 3-D imaging used for volunteers and patients.

Fast imaging with steady-state free precession (TrueFISP) modulus images are acquired as a retrospective electrocardiogram (ECG) gated scan with reconstruction of 40 images per RR-interval, slice thickness 6 mm, repetition time (TR) 26 ms, echo time (TE) 1 ms, flip angle (FA) 80°, field of view (FOV) 240 mm × 320 mm and matrix size 192 × 256 pixels adjusted to body habitus to avoid ghosting artifacts (pixel size 1.25 mm × 1.25 mm).

Fast Low Angle Shot (FLASH) 2-D phase-contrast images were acquired as a retrospective ECG gated scan with reconstruction of 40 images per RR interval, slice thickness 6 mm, TR = 61 ms, TE = 3 ms, FA = 30°, velocity encoding (VENC) of 150 cm/s, where the matrix size and slice position were adjusted to the TrueFISP image allowing their mapping.

The 3-D MR structural images of healthy volunteers were acquired using the Half Fourier Acquisition Single Shot Turbo Spin Echo (HASTE, properties: slice thickness 6 mm, TR = 700 ms, TE = 26 ms, FA = 160°, FOV 233 mm × 340 mm and a matrix of 176 × 256 pixels adjusted to a body habitus, pixel size 1.32 mm × 1.32 mm) technique on a 1.5 T scanner using a high inter-slice spacing of 6.6 mm without injected contrast agent, yielding low quality “black-blood” images (see Fig. 1). The black-blood aorta images pose a hard segmentation problem due to unclear boundaries between the aorta and surrounding organs (veins, heart and lungs). However, the advantage of such scanning process is the increased acquisition speed with a non-invasive approach.

The 3-D MR structural images of patients were obtained using Fast Low Angle Shot (FLASH, properties: slice thickness 0.9 mm,

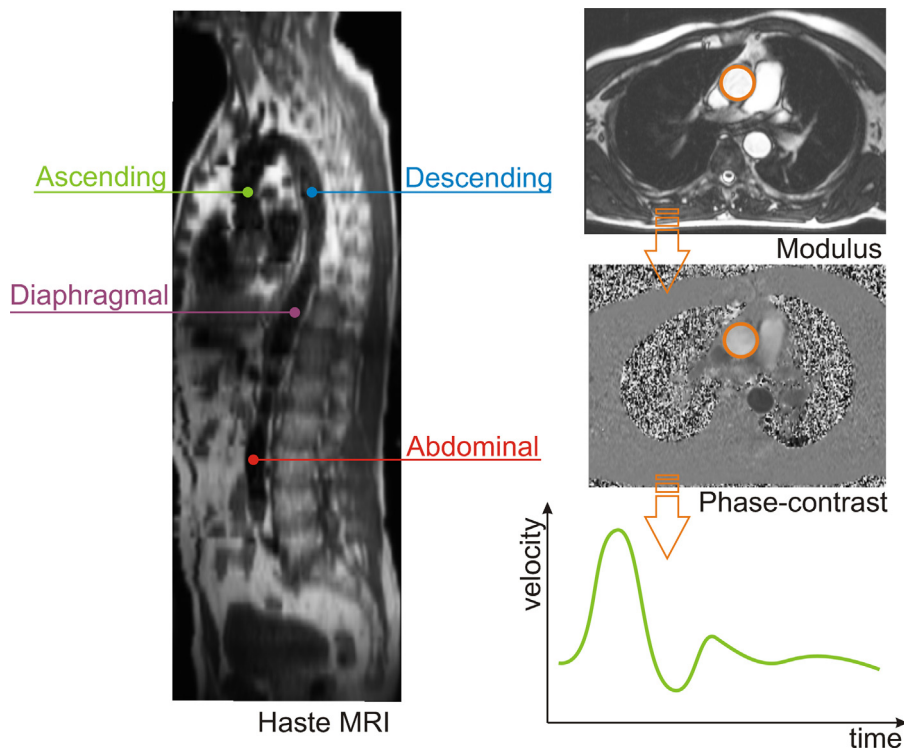


Fig. 1. The 3-D HASTE MRI data set of a healthy volunteer (“black-blood” images) with marked cardiac axes at the ascending, descending, diaphragmal and abdominal level. At each level the modulus images need to be segmented and used as a mask for velocity calculation on phase-contrast images in order to obtain the pulse wave.

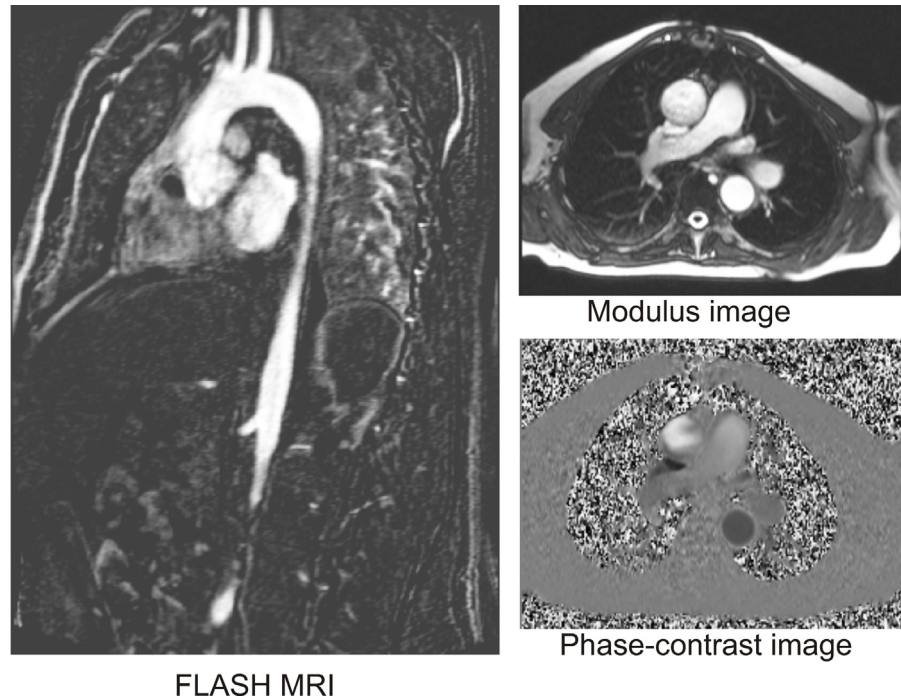


Fig. 2. A Marfan syndrome patient data set. Left: the 3-D FLASH MR data set of a patient obtained by subtracting the contrast-enhanced data set with the non-contrasted scan in order to obtain clear images of an aorta as shown in Fig. 2. All the subject gave their consent to their inclusion in this study.

TR = 3.8 ms, TE = 1.3 ms, FA = 20°, FOV 299 mm × 399 mm and a matrix of 288 × 384 pixels adjusted to body habitus, pixel size 1.03 mm × 1.03 mm) technique on a 1.5T scanner by subtracting the contrast-enhanced data set with the non-contrasted scan in order to obtain clear images of an aorta as shown in Fig. 2. All the subject gave their consent to their inclusion in this study.

Fig. 3 shows the block diagram of our proposed algorithm decomposed into three major parts representing the main contributions of this paper. The left column represents the centerline extraction algorithm, the central column shows the algorithm for segmenting modulus images, while the column on the right represents the pulse wave analysis method. The PWV is measured by

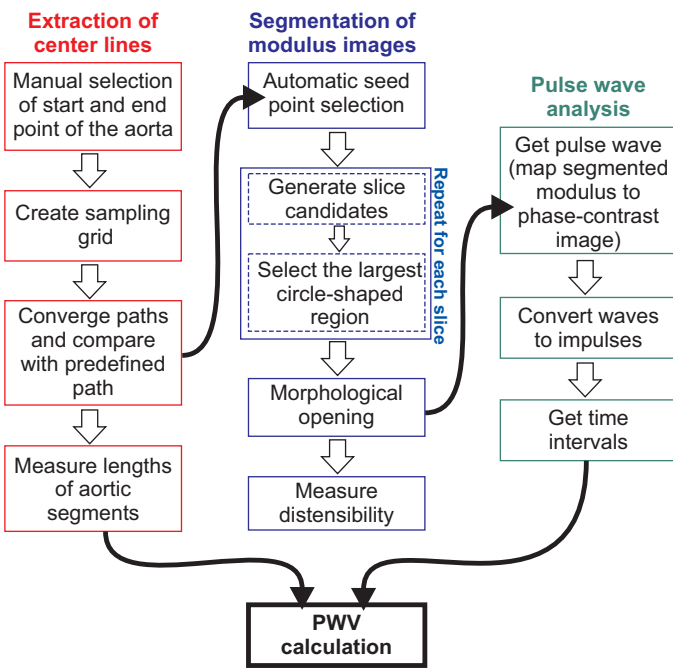


Fig. 3. Block diagram of the proposed algorithm.

“tracking” the propagation of the pulse wave from the ascending level to the abdominal level to determine the transition time. For this the aortic region in the modulus images is segmented and the obtained result is used as a mask for the mean velocity calculation in phase-contrast images as depicted in Fig. 1. The length of the aorta between each of the levels is obtained by extracting the centerline from 3-D MRI images and is used in combination with the obtained propagation time intervals to obtain the speed of the pulse wave, which is the PWV. Another important parameter is the distensibility of the aortic wall, which is represented through the

maximum, minimum and average circumference of the aortic wall calculated for each aortic level.

2.2. Aorta centerline extraction

In this Subsection we describe our proposed algorithm for extracting the centerline of the aorta, as depicted in the left column of the block diagram in Fig. 3. The extraction of the aortic centerline is a necessary step in the PWV calculation in order to obtain the length of the aortic vessel between the four levels of the aorta. Our goal is to create a general algorithm applicable for both contrast-enhanced and “black-blood” MRI images. The black blood aortic images pose a hard segmentation problem [26] due to their low quality with high presence of artifacts and a high inter-slice spacing of 6.6 mm (pixel spacing is 1.32 mm × 1.32 mm), which often causes the effect of a single object not being connected in the neighboring slices. Fig. 4 illustrates artifacts found in the “black-blood” MRI data sets, where the aorta is not clearly visible in a number of adjacent slices due to blood flow. For this reason, the centerline extraction method has to be robust, while requiring as little user interaction as possible.

The main idea of our approach is to build a structured grid graph, where node and link values are sampled from the image. The centerline of the aorta is extracted in a semi-automatic way, where the user has to specify the start and end point of the aorta. We design our algorithm to allow a quick examination of multiple alternative paths for the extraction of complicated vessel structures.

2.2.1. Creating the sampling grid

In order to eliminate the influence of artifacts that randomly appear in certain slices of black-blood MRI images of abdomen we propose construction of a sampling grid that takes into account only the “valid” candidate positions of the aorta. Nodes of the grid will be positioned only at those pixels which can belong to the region of the aorta (e.g. in case of MRI images the aorta is dark, and therefore, the grid nodes will be positioned at the darkest pixels in a predefined manner). We create an initial regular structured grid (graph) of an arbitrary size, whose nodes are equally distributed with a

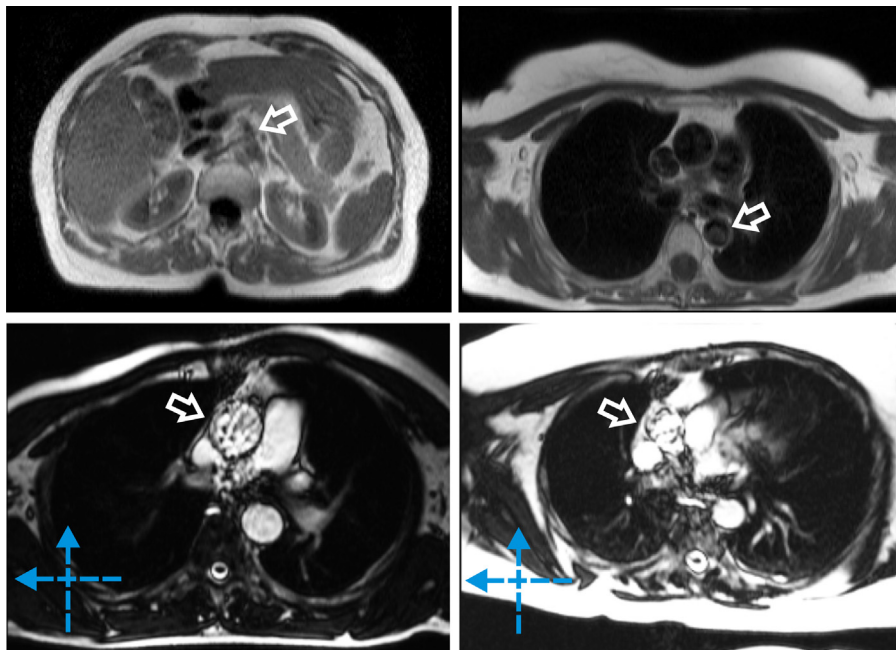


Fig. 4. Artifacts found in CMR images indicated with outlined white arrow. Top row shows images from HASTE data set. Left: the aorta is not visible in the transversal slice at the diaphragmal position, right: noise in the descending aorta. Bottom row: images from TrueFISP data set of the ascending aorta affected by artifacts. Only two directions of line-shaped structuring elements (SE) are used for the segmentation (dashed arrows).

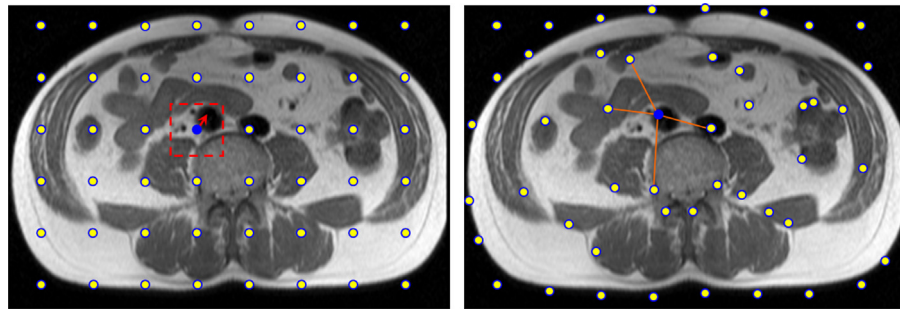


Fig. 5. Illustration of a 2-D sampling grid. Left: regular grid with many nodes (yellow circles) placed at “invalid” bright regions. Nodes are repositioned in the region defined as the half of the node spacing in each direction (illustrated for a blue circle repositioned inside the dashed square). Right: repositioned nodes in the darkest regions. Links between adjacent nodes form a grid (illustrated for a single node).

constant spacing in each direction (x , y and z directions). The node spacing is determined by the user specified number of sampling nodes in each of directions. Our experiments show that sampling grid of dimensions $25 \times 25 \times 25$ results in a sufficiently good balance of given results and required processing times. Advantage of the sampling approach is reduced processing times compared to techniques that process every voxel of the 3-D image.

Since the nodes in the initial grid are regularly distributed, some of them are situated in bright regions of the MRI image, which are not likely to be regions of the aorta. For this reason it is of interest to move the nodes to the pixels which can be parts of the aorta. However, in order to maintain a relatively regular distribution of the nodes, we can reposition the nodes only in the region up to the half of the node spacing in each direction. This principle is illustrated in Fig. 5 for a 2-D case. This method ensures that the nodes will not overlap after repositioning, while we increase the possibility that they fall in a region of the aorta. This means that our algorithm searches for the darkest region around each node (search areas do no overlap). We will now explain the method for defining the darkest regions in the image.

Let us consider a dark pixel in the image. We want to determine to what size of a 2-D equidistant neighborhood is the pixel darker than its considered neighborhood. Therefore, we compare the gray value of the pixel to the average pixel gray value of the 2-D neighborhood. The new pixel gray value will be the size r of the 2-D neighborhood for which the pixel gray value is lower than the neighborhood average gray pixel value for all smaller neighborhoods with size $r' \leq r$. Let us consider a ring-shaped circular (equidistant) 2-D neighborhood of the pixel. Finding the average of all pixel values in such a neighborhood resembles the *spherical mean*. The spherical mean operator of a function at a point is the average of all values of the function on a sphere (ring in 2-D case) of given radius centered at that point. Since we consider a multiscale 2-D approach, we actually compare the pixel value to its spherical means of a 2-D function (image) for different radii r values.

Let $\mathbf{p} \in \mathbb{Z}^2$ denote the pixel coordinates in a 2-D discrete image g with pixel gray value range $[0, 255]$. For given pixel coordinates \mathbf{p} we define a set of equidistant pixels at a radius $r \in \mathbb{N}$ as:

$$S_r(\mathbf{p}) = \{\mathbf{q} \in \mathbb{Z}^2 : (r - 1)^2 < (x_{\mathbf{q}} - x_{\mathbf{p}})^2 + (y_{\mathbf{q}} - y_{\mathbf{p}})^2 \leq r^2\} \quad (1)$$

For this set the average of all pixel values can be expressed as:

$$\mu_r(\mathbf{p}; g) = \frac{1}{|S_r(\mathbf{p})|} \sum_{\mathbf{q} \in S_r(\mathbf{p})} g(\mathbf{q}), \quad (2)$$

where $|S_r(\mathbf{p})|$ denotes the number of pixels in the equidistant neighborhood and $g(\mathbf{q})$ denotes the pixel gray value.

The new pixel value will be a size r of the 2-D neighborhood for which the pixel value is lower than the neighborhood average pixel value $\mu_r(\mathbf{p})$ for all smaller neighborhoods with size $r' \leq r$:

$$\rho(\mathbf{p}; g) = \max\{r : g(\mathbf{p}) \leq \mu_{r'}(\mathbf{p}; g) \text{ for every } r' \leq r, r' \in \mathbb{N}\}. \quad (3)$$

Finally, we define the position of the darkest region as the position of the pixel with the gray value belonging to the lowest 10% of all searched values in the given node area, which has the highest transformed value $\rho(\mathbf{p}; g)$, as defined in (3). In this fashion we combine the pixel intensities with the range of influence of their neighborhoods, which constitute valid candidates for aortic regions. When the position of the darkest region for a given node is located, the node of the grid is moved to the found position. In this fashion, we reposition all the nodes to the darkest regions while making sure that the nodes do not overlap. We finalize the grid construction by entering values for the links connecting each node to its six closest neighbors from the initial grid. The cost of a link $m(L)$ is calculated as the average of all the pixel intensities belonging to the line segment set L connecting the two nodes of the link:

$$m(L) = \frac{1}{|L|} \sum_{i=1}^{|L|} g(\mathbf{p}_i), \quad (4)$$

where $g(\mathbf{p})$ represents the gray value of the pixel \mathbf{p} . Fig. 6(a) shows the modified grid of size $25 \times 25 \times 25$, where the red color indicates higher link values and blue indicates lower link values.

2.2.2. Center line extraction

The centerline extraction algorithm is depicted in Fig. 6. In order for the centerline to be extracted, the user must specify the start and the end position of the desired centerline path. These positions are entered into the existing sampling grid as new nodes, which we connect with their closest six nodes and enter their link costs as described by (4). We use the link costs of the sampling grid to converge the graph using Dijkstra's shortest path algorithm [38] with respect to the entered start and end nodes separately. This means that each of the nodes contains the shortest distance and path to both the user selected start and end node. In this fashion, the final metric for each of the nodes m_N is calculated as the sum of distances from both the start and end node:

$$m(N) = l(N, N_{start}) + l(N, N_{end}), \quad (5)$$

where $l(N_1, N_2)$ represents shortest path between the given nodes (obtained using the Dijkstra's shortest path algorithm). All distinct paths between the start and end nodes are calculated by going through all grid nodes and extracting paths to start and end node while keeping track which paths have already been considered. In order to obtain only distinct paths, nodes that are a part of already found paths are not taken into account. The found distinct paths are

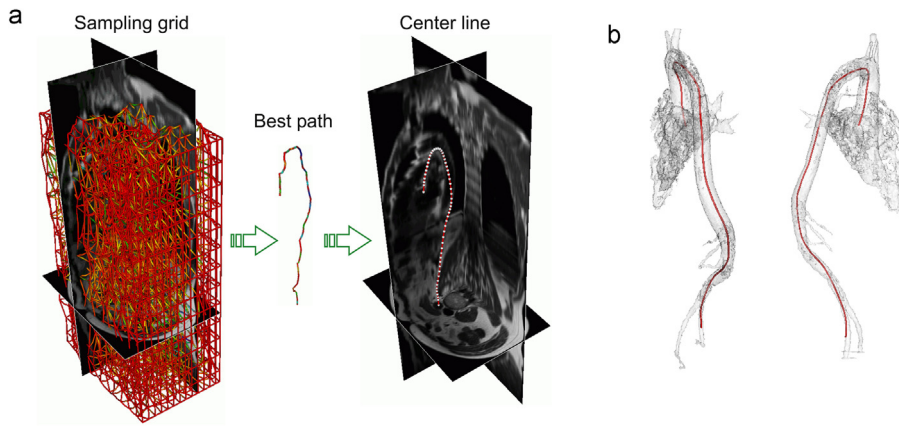


Fig. 6. Illustration of the sampling skeleton grid construction and the center line extraction. (a) Left: the final sampling grid, center: calculated (intermediate) best path, right: the aortic center line (smoothed best path). (b) Extracted centerline from a single Marfan syndrome patient data set.

sorted in an ascending order based on the calculated path metrics. Finally, the obtained paths are smoothed as shown in Fig. 6(a). Fig. 6(b) shows an extracted centerline for a Marfan syndrome patient where contrast enhanced MR images were used.

Our algorithm can be used with a predefined aortic model. In this case the direction of each link in the sampling grid is compared to the corresponding segment on the predefined aortic path. The corresponding segment is determined by projecting the point situated at the middle of the link line segment to the segments of the predefined model. The corresponding segment is the one where the projection falls on the segment while having the shortest distance from the given (original) link line segment. This way the directions of the link and its corresponding segment on the predefined model are compared and used as a weighting factor for link costs:

$$w(L; S_L) = 1 - \cos(\alpha(L, S_L)), \quad (6)$$

where $\alpha(L, S_L)$ denotes the angle between the link L and its corresponding model segment S_L . In this case, the link metric is:

$$m_w(L) = w(L; S_L)m(L). \quad (7)$$

It should be noted that in the case of contrast enhanced images, the priority will be given to brighter pixels and image regions, unlike in the case of "black-blood" images, where the priority is assigned to dark regions of the image.

The first column of the block diagram in Fig. 3 shows the implementation of our proposed robust aorta center line extraction method by creating the sampling grid using image characteristic values. The default size of the sampling graph is set to $25 \times 25 \times 25$ nodes, although the user can specify the sampling grid of any dimensions. The user is required to manually select the start and end positions of the aorta, after which the sampling graph is created and the best path is extracted. We implement our application in such a way that the user can scroll through all the possible found paths and select the one that he finds the most suitable (however, in 80% of cases, the automatically selected path is the optimal one).

2.3. Segmenting modulus images

This Subsection describes our proposed algorithm for the segmentation of modulus images, as presented in the middle column of the block diagram in Fig. 3. Although there can be considerable motion in the aorta during the cardiac cycle, most of segmentation algorithms are able to deal with the aortic motion. However, the exact segmentation of the aortic wall is a hard segmentation problem due to artifacts (see Fig. 4). Hence, we propose a robust segmentation method using projections, where the current pixel

value is compared to the characteristic value of the projection. The projection is defined using a line-shaped structuring element (SE):

$$L_n = \left\{ \mathbf{p} \in \mathbb{Z}^2 : y_{\mathbf{p}} = k(n)x_{\mathbf{p}} \right\}, \quad (8)$$

where $x_{\mathbf{p}}$ and $y_{\mathbf{p}}$ denote pixel coordinates and $k(n)$ denotes the function of the line angle determined by the parameter n :

$$k(n) = \tan\left(n \frac{\pi}{n_{max}}\right), \quad n \in [1, \dots, n_{max}]. \quad (9)$$

This yields n_{max} number of line-shaped SEs, with the constant angle between the neighboring lines.

In order to characterize the neighborhood (defined by the SE), different operators were applied to the whole set of values from the image, defined by the SE. Let $g(\mathbf{p})$ be the gray value at position \mathbf{p} and let:

$$f^{(i)}(n, \mathbf{p}) \triangleq \text{opr}^{(i)} g(\mathbf{p} + \mathbf{p}') \quad \forall \mathbf{p}' \in L_n \quad (10)$$

have the following meaning: $\text{opr}^{(i)}$ is the name of the operator. The superscript (i) refers to which operator we are talking about, e.g. for $i=1$ we may have: $\text{opr}^{(i)} = \min$. Hence, the operator is applied to the set of values defined by the line-shaped SE centered at the position \mathbf{p} .

Similarly to (3), the new pixel gray value will be the number of directions for which the current pixel gray value is higher than the gray value calculated for the given operator:

$$\lambda(\mathbf{p}; f^{(i)}) = |\{n : g(\mathbf{p}) \geq f^{(i)}(n, \mathbf{p})\}|. \quad (11)$$

In this fashion we measure the brightness of the current pixel by comparing it to the characteristic gray value of its wider neighborhood (defined by the line-shaped SE). The transformed image is thresholded to obtain the final segmentation. In this paper we use two directions of line-shaped SEs ($n_{max} = 2$) and we threshold the transformed image with the highest possible threshold value. The main idea behind this principle is to use various operators to obtain different segmented images, after which the best segmentation result is selected based on predefined criteria. A variety of profile operators can be obtained by an aggregation step on a set of predefined base operators B :

$$f_C(n, \mathbf{p}) = \frac{1}{d} \sum_i f^{(i)}(n, \mathbf{p}), \quad (12)$$

where d represents the number of base operators involved in generating the combined operator f_C . In this paper we use the following base operators: mean, minimum, maximum, mid-range (average

of the minimum and the maximum value) and the square root of multiplied minimum and maximum values. In our previous work [34,33], the listed operators have proven effective for obtaining various segmentation results, although the user may specify any other operator (defined on a set of values) as well, where the total number of operators is also user defined (e.g. median can also be used as a base profile operator, but we avoid its use due to required array sorting which prolongs processing times).

As mentioned earlier, the main idea of our approach is to generate a number of candidate regions (as possible correct aorta segmentation results) by using a number of various operators (total of 31 operators) obtained from the set of base operators using (12). Each operator produces a different segmentation candidate region and the final result is obtained by selecting the most round and large enough candidate region. This is done by grading each segmented area according to their circularity and size constraints (depending on the expected size of the aorta). The advantage of this approach is that the segmentation method is not constrained by an assigned predefined shape of the aorta. Instead, our algorithm is capable of segmenting various aortic shapes by generating candidate regions, from which the most appropriate aortic region is later selected. It should be noted that the circularity and size criterion do not “guide” the segmentation, just the candidate selection process (if the aorta is not circular, each operator will yield a non-circular segmentation). Vessel regions in TrueFISP images have sufficient contrast in comparison to surrounding tissues. Hence, we use only 2 projection directions as illustrated in Fig. 4. The user specified seed point is required only in case all data sets are being processed in parallel. Otherwise, the calculated centerline can be used for the seed point initialization. To insure the smoothness of the final segmentation, morphological opening of the whole segmented volume is performed after the candidate selection. Segmented TrueFISP images are depicted in Fig. 7, where the segmented modulus sequence is represented as a 3-D volume, enabling us to easily observe the evolution and movement of the aortic wall at the given level over time.

Optionally, the region of interest can be defined to limit the volume of the image processed by our algorithm. The default value of the ROI is set to 50 mm, which is higher than the normal diameter of the aorta, insuring that the region of the aorta falls inside the ROI.

2.4. Pulse wave propagation

The method described in this Subsection is represented as the right column of the block diagram in Fig. 3. After the successful segmentation of modulus images, we calculate the pulse wave for each of the aortic positions as an average value of pixels of phase-contrast images masked by the corresponding segmented modulus

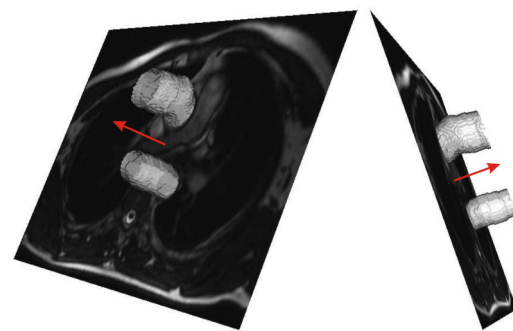


Fig. 7. Segmented regions of the ascending and descending aorta on a single True-FISP data set, where the models represent the variation of a 2-D region over time (arrows indicate time transition). The ascending aortic region varies in position and area, while the descending aorta has only a small variation in its area.

regions (see Fig. 1). In our case the pulse wave consist of 40 samples for each aortic position (40 slices), as depicted in Fig. 8, where full lines represent pulse waves at the ascending, descending, diaphragmal and abdominal position. It should be noticed that different time intervals exist between the observed pulse waves, which will (in combination with calculated lengths of the aorta) define the speed of the pulse wave (the pulse wave velocity). During the transition the pulse wave is deformed [39] (e.g. compare the ascending and the abdominal wave in Fig. 8), which raises a question on how to determine the exact moment when the wave passes through a given aortic position.

The experience has shown that the steepest slopes (especially, the upslope) are the wave characteristics which are the least influenced by the wave deformation [40], resulting in the impulse representation of the pulse wave. The impulse representation can be defined as an impulse that best illustrates the start and end of the pulse wave, consisting of steepest slopes and a constant “base” value, where the intersection of the steepest slope and the base value defines the starting point of the impulse (see Fig. 8). Obviously, the impulse start instant depends on the calculation of the base value, for which various approaches exist (e.g. some methods take the median value of the whole pulse wave or the average of a predefined number of its last samples). However, the listed approaches often highly depend on the number of total samples or on the number of samples taken into account.

We propose a new approach to calculate the arrival time of the pulse wave. Our method uses the steepest slopes and introduces a novel approach for determining the base of the impulse representation. The steepest slopes are determined as the largest difference in consecutive wave values for the rising and the falling edge. We define the base of the impulse representation as the average value

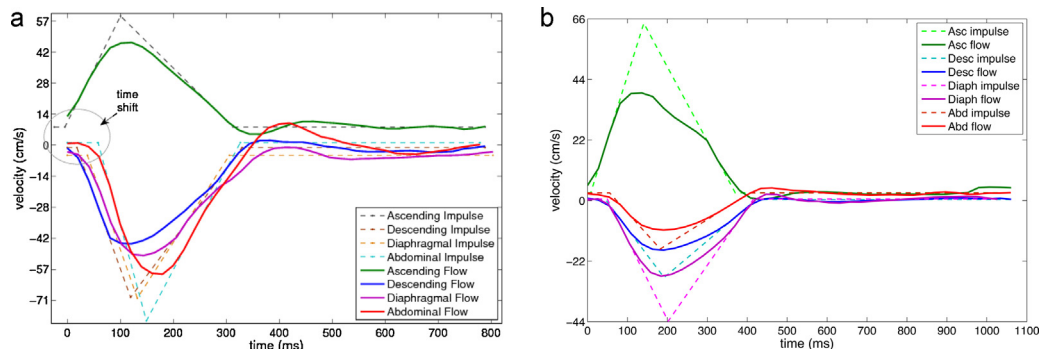


Fig. 8. The pulse wave propagation. Full lines represent pulse waves and dashed lines their corresponding impulse representations. Left: time interval between the pulse waves is calculated as the time interval between the start of the first slopes of their corresponding impulses. Right: Marfan patient pulse waves are deformed, with small time intervals between them, yielding high PWV values.

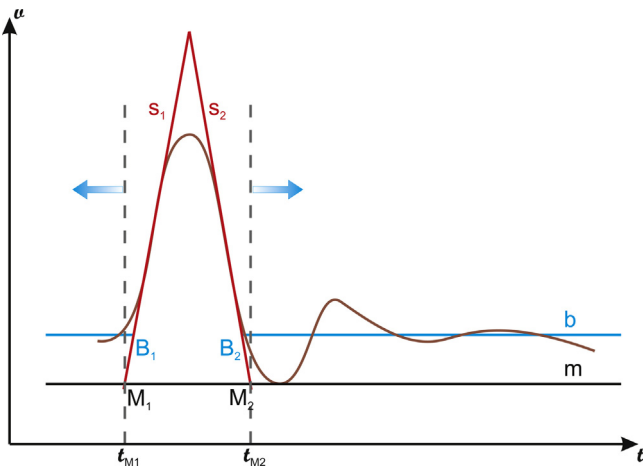


Fig. 9. The impulse representation of the pulse wave. The wave minimum value m , the steepest slopes (s_1 and s_2) and their intersections M_1 and M_2 are determined. The base value b is the average of all samples outside the range of projected intersections (t_{M1} and t_{M2}). The impulse start instance B_1 is determined by an intersection of the first steepest slope s_1 and the base value b .

of all wave samples that do not belong to the range of the slopes, determined by intersections of the steepest slopes with the wave minimum (or the maximum) value (see Fig. 9). The algorithm starts by calculating the steepest slopes s_1 , s_2 and the wave minimum value m . The average of all samples that are not in the interval of projected intersections of steepest slopes and minimum value on the x axis (t_{M1} and t_{M2}) are used to obtain the base value b . The intersection of the first steepest slope s_1 and the base value b determines the impulse start instant B_1 . Note that the second slope is only used to specify the range for the base value calculation. Fig. 8 shows the obtained pulse waves at different aortic positions and their corresponding impulse representations. The time interval needed for the pulse wave to pass from one aortic position to another is determined as a time shift between the impulse representations of the corresponding pulse waves. A good property of our approach is its invariance to the number of wave samples, constituting a robust method for creating impulse representations. Another advantage of this method is that it uses both steepest slopes in the calculation, thus taking into account the deformation of the pulse wave during transition.

The last step of our proposed algorithm calculates the PWV values from obtained time intervals and lengths of aortic segments.

3. Results

In order to demonstrate the need for a robust centerline extraction method for HASTE MRI images, we compare the obtained centerline with the results of various aorta segmentation methods, as shown in Fig. 10.

The segmentation result using the method of [27] (MiaLite application) is either not connected (see Fig. 10(a)) or “leaks” into neighboring regions (even with selecting six seed and blocking points). The segmentation result obtained using ITK-SNAP [28] in Fig. 10(b), shows an incomplete segmentation result of the aorta, although six seed points have been placed to cover each aortic region. Setting higher parameters for contour boundary movement created leaks (although smoothness parameter was increased to prevent leaking). The segmentation result of [31] (implemented in 3D Slicer) method depicted in Fig. 10(c), shows relatively small leak regions (however, the leak regions are large enough to influence accurate centerline calculation), where six seed points and fine contour parameter tuning were needed to obtain the segmentation. None of the described segmentation methods yield sufficiently

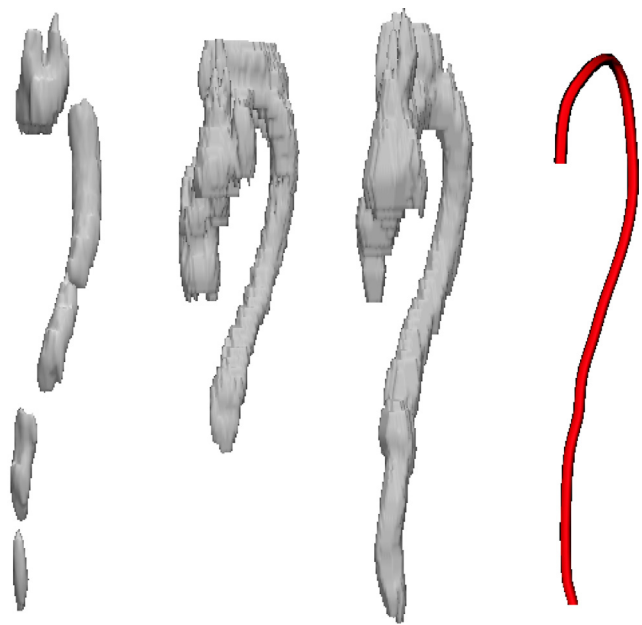


Fig. 10. The segmentation and aortic centerline extraction of the HASTE MRI data. (a) MiaLite [27], (b) ITK-SNAP [28], (c) robust statistics driven active contours from 3D Slicer [31], (d) our proposed centerline extraction method.

good segmentation result for an accurate centerline extraction. Finally, Fig. 10(d) shows the aortic centerline extracted using our proposed method. The centerline is accurate due to positioning grid nodes to valid positions and interconnecting them.

We perform a sensitivity analysis by shifting the initial sampling grid by half of the grid size in x and y directions. The largest obtained difference in the aortic centerline length is 5.1 mm (423.3 mm compared to 428.4 mm) in case the length of the whole aorta is measured, which is small enough, proving that the sufficiently dense sampling grid was used.

We compare the calculated lengths between the given aortic levels obtained using our method with the aortic lengths of manually determined centerlines by an expert (centerlines were drawn in the 3-D application of the Siemens MR workstation). The results presented in Table 1 show the average values and standard deviations for all 22 HASTE data sets. The results show good correspondence between measured and manually determined lengths, where the highest average difference of 7 mm was obtained for the aortic segment between the descending and diaphragmal aorta, while the differences in lengths of other segments are significantly smaller.

We compare our modulus image segmentation results with the manually determined expert segmentation for images of the ascending aorta where artifacts were present. For this purpose we use the Dice coefficient [41], which is a set similarity measure

Table 1
HASTE MRI center line length comparison.

Center line lengths (mm)	Mean	S.D.
Asc-Desc manually det.	115.81	22.13
Asc-Desc our method	110.47	20.13
Desc-Diaph manually det.	107.13	17.08
Desc-Diaph our method	99.76	17.52
Diaph-Abd manually det.	173.22	19.23
Diaph-Abd our method	179.48	19.24

Table 2

The ascending level TrueFISP image segmentation under influence of artifacts. Comparison of the Dice coefficients, radii estimated from aortic areas of expert and our segmentation and the ratios of the given radii.

<i>n</i>	Dice	Our <i>r</i> (mm)	Expert <i>r</i> (mm)	<i>r</i> ratio
1.	0.91	16.43	17.79	0.92
2.	0.89	11.56	12.8	0.9
3.	0.93	15.8	16.9	0.93
4.	0.91	11.5	12.49	0.92
5.	0.64	15.17	16.62	0.91
6.	0.91	13.2	14.5	0.91
7.	0.86	11.86	13.54	0.87
8.	0.85	11.1	12.8	0.86

Table 3

The segmentation of the aortic region for healthy volunteers. Comparison of measured areas, circumference and radii estimated from the area and the circumference.

Aortic level	<i>a</i> (mm ²)	<i>c</i> (mm)	<i>r_a</i> (mm)	<i>r_c</i> (mm)
Ascending	676.18	117.43	14.67	18.69
Descending	402.56	90.24	11.32	14.36
Diaphragmal	322.35	80.85	10.13	12.87
Abdominal	155.96	56.03	7.04	8.92

defined as twice the ratio of intersection of two sets and the number of elements contained in both of them:

$$s(A, B) = \frac{2|A \cap B|}{|A| + |B|}, \quad (13)$$

where one set represents the set of segmented pixels and the other one the set of ground truth pixels. The results of the comparison are given in **Table 2** for 8 TrueFISP data sets containing severe artifacts in the region of the ascending aorta. High Dice coefficient values (all above 0.85, except one) indicate high accuracy of our segmentation method. The radius of the aorta was estimated through the calculated aortic area, where the circular aortic wall shape is assumed. The radii of the aorta calculated using our proposed method and the manual segmentation by an expert differ in approximately 1 mm and the ratio of these values is almost constant in all examined cases. This makes it possible to estimate the radius measured by an expert by multiplying the radius value obtained using our algorithm with the average calculated ratio which equals 0.9 (this is possible even in the case of the lowest calculated Dice coefficient, since the ratio of radii in that case is 0.91). The aortic area and radii results obtained on the TrueFISP images of healthy volunteers are presented in **Table 3** for all aortic levels. The results compare average values of aortic area *a*, circumference *c* and radii estimated from the aortic area *r_a* and circumference *r_c*. It should be noted that all values decrease from the ascending to the abdominal level, which is in accordance with the expected results, showing the correctness of the proposed segmentation method. The aortic region area and radii results obtained on modulus images of Marfan syndrome patients are presented in **Table 4**.

Finally, in order to validate the measured pulse wave velocities, we compare our PWV results to the validated software FLOW and an in-house developed and validated PWV calculation tool (LUMC, Leiden, Netherlands). The aortic centerlines of healthy volunteers

Table 4

The segmentation of the aortic region for Marfan syndrome patients. Comparison of measured areas, circumference and radii estimated from the area and the circumference.

Aortic level	<i>a</i> (mm ²)	<i>c</i> (mm)	<i>r_a</i> (mm)	<i>r_c</i> (mm)
Ascending	490.750	99.875	12.5	15.9
Descending	396.125	86.875	11.23	13.83
Diaphragmal	268.875	73.375	9.25	11.68
Abdominal	218.000	64.250	8.33	10.23

Table 5

Healthy volunteers PWV comparison.

PWV (m/s)	Mean	S.D.
Asc-Desc LUMC	5.14	2.51
Asc-Desc our method	5.3	2.47
Desc-Diaph LUMC	6.92	5.55
Desc-Diaph our method	6.14	6.58
Diaph-Abd LUMC	6.71	3.69
Diaph-Abd our method	6.8	2.14
Asc-Abd LUMC	5.23	1.45
Asc-Abd our method	5.45	1.42

Table 6

Marfan syndrome PWV comparison.

PWV (m/s)	Mean	S.D.
Asc-Desc LUMC	5.06	1.85
Asc-Desc our method	6.3	1.34
Desc-Diaph LUMC	13.66	14.96
Desc-Diaph our method	10.99	12.47
Diaph-Abd LUMC	8.58	7.47
Diaph-Abd our method	8.26	7.23
Asc-Abd LUMC	6.37	2.2
Asc-Abd our method	6.38	2.33

(black-blood HASTE MRI images) were manually delineated by an expert in the 3-D application of the Siemens MR workstation. The expert used a few methods for the analysis of the pulse wave in the PWV tool application (see [Section 2.4](#)) in order to obtain the most realistic values of the PWV. The comparison of obtained PWV values of 22 healthy volunteers for different aortic segments using the validated software and our application are presented in [Table 5](#). The comparison of PWV results for 8 Marfan syndrome patients are presented in [Table 6](#).

Our calculated PWV values correspond very well to the calculated PWV values of the validated software. Moreover, the calculated values fall inside the range of expected values of PWV for each of the aortic segments of healthy volunteers [42], proving the correctness of the proposed method. The calculated PWV values for Marfan syndrome patients show higher values (in comparison to healthy volunteers) in the part of the aorta between descending and diaphragmal level, as well as slightly higher values for the part of the aorta between diaphragmal and abdominal level. The expected PWV values for Marfan syndrome patients are higher than in the case of healthy volunteers, which again verifies the correctness of the proposed method.

4. Discussion

To determine the pulse wave propagation times, we use impulse representation method that takes into account both steepest slopes of the pulse wave (see [Section 2.4](#)). It is well known that the down-slope (the second slope) of the pulse wave is often affected by wave reflections. However, this does not significantly affect the impulse modeling in our approach because the second slope of the impulse is only used to determine the range of values that are not included for calculation of the impulse representation base value. Independently of the quantity of wave reflections, the end of the second slope always defines the range of values where the wave goes into "relaxation", which is an important factor in the calculation of the impulse representation base value. The upslope (the first steepest slope) and the base value define the start of the modeled impulse, where the upslope is not significantly affected by reflected waves [43]. Hence, our proposed method of impulse modeling is robust to wave reflections.

In our case the TrueFISP scans use a much shorter acquisition window than the acquisitions for phase-contrast images, which

often implies that lumen area in modulus images is over-estimated. This can be observed by mapping the aortic regions of modulus images to the corresponding phase-contrast images. Hence, the aortic region in TrueFISP image needs to be slightly under-segmented (a smaller region needs to be taken into account) in order to map well to the aortic region in the phase-contrast image. This has been solved by our segmentation method using projections (line-shaped SEs) with selecting the most circular aortic region candidate as the final segmentation result (see Section 2.3). Due to the radial positioning of projections (line-shaped SEs) when observed from the currently processed pixel, our approach gives priority to circular objects while excluding its edges. This means that the obtained aortic region from the TrueFISP image is slightly under-segmented, which is a benefit when mapping to phase-contrast image for velocity calculation. This is supported by the measurements in Table 2, where the expert aortic region segmentation area is always slightly larger than in the case of our proposed method.

The PWV average and standard deviation values between the descending and the diaphragmal levels of the aorta are higher than in the other aortic segments (both for LUMC and our proposed method). This is most likely the result of centerline length calculation. The descending-diaphragmal segment of the aortic centerline often contains a saddle point. The pulse wave propagation might not follow the exact centerline (as determined by our method or by an expert), which can, in turn, cause deviation from expected PWV values.

Our method should be applicable to calculating PWV for any other vessel where TT MRI approach is commonly used. The segmentation and centerline extraction algorithm could be easily modified for application to other data sets (e.g. 4-D data). Compared to the other PWV calculation methods, our method exhibits the general advantages and disadvantages of a cross-sectional TT approach. Our method uses more data sets compared than the QA approach [13] (that uses a single cross-sectional sequence), but yields higher accuracy because it is not as dependent on the exact segmentation of the aortic region. Similarly, the proposed method uses more data sets than multisite TT method [14], but is less sensitive to variations in flow (a single para-sagittal slice can contain aortic flow variations). Our PWV calculation approach uses automatic pulse wave transit time measurement as well as XC method [15], with the difference that we give priority to curve upslope, rather than to the whole velocity curve (which is the case with the XC approach). The performance of our algorithm was tested on a 2GHz CPU. The calculation of centerlines and the length measurement last approximately 1.5 min for the HASTE data set of dimensions $120 \times 180 \times 256$. The segmentation of modulus images depends on the size of the aortic region that is being segmented and the volume defined by the region of interest, lasting from 0.5 to 2 min (the average time is approximately 1.3 min) for series of 40 slices (dimensions 192×256). Note that the segmentation can be performed in parallel for each aortic level, while the method would benefit from implementation on a graphics processing unit (GPU).

5. Conclusion

We introduced in this paper a novel tool for the aortic pulse wave velocity (PWV) measurements on magnetic resonance (MR) images. We have designed an effective aortic region segmentation and center-line extraction algorithm, with an optional use of a predefined aortic model. The extracted centerlines and segmented aortic regions were compared to the expert segmentation, showing sufficient accuracy of our proposed methods. We introduced a novel method for analysis of the pulse wave by taking into account the steepest slopes and deformation of the pulse wave over time in order to obtain a robust automatic method. The pulse wave

velocity measurement on 22 healthy volunteers shows good correspondence to the results obtained by validated PWV measurement software (FLOW and LUMC PWV tool). The calculated PWV values fall in the range of values which are expected in case of healthy volunteers. The PWV measurements on 8 Marfan syndrome patients also correspond to the measurements performed with the validated software, while showing other range of values compared to the healthy volunteers.

References

- [1] Brandts A, van Elderen SGC, Westenberg JJM, van der Grond J, van Buchem MA, Huisman MV, et al. Association of aortic arch pulse wave velocity with left ventricular mass and lacunar brain infarcts in hypertensive patients: assessment with MR imaging. *Radiology* 2009;253(3):681–8.
- [2] Groenink M, de Roos A, Mulder BJ, Spaan JA, van der Wall EE. Changes in aortic distensibility and pulse wave velocity assessed with magnetic resonance imaging following beta-blocker therapy in the Marfan syndrome. *American Journal of Cardiology* 1998;82(2):203–8.
- [3] Kröner E, van der Geest R, Scholte A, van den Boogaard P, Hendriksen D, Kroft L, et al. Evaluation of sampling density on the accuracy of aortic pulse wave velocity from velocity-encoded MRI in patients with Marfan syndrome. *Journal of Cardiovascular Magnetic Resonance* 2012;14(6):1470–6.
- [4] Roes SD, Alizadeh Dehnavi R, Westenberg JJ, Lamb HJ, Mertens BJ, Tamsma JT, et al. Assessment of aortic pulse wave velocity and cardiac diastolic function in subjects with and without the metabolic syndrome. *Diabetes Care* 2008;31(7):1442–4.
- [5] van Elderen SG, Brandts A, van der Grond J, Westenberg JJ, Kroft LJ, van Buchem MA, et al. Cerebral perfusion and aortic stiffness are independent predictors of white matter brain atrophy in type 1 diabetic patients assessed with magnetic resonance imaging. *Diabetes Care* 2011;34(2):459–63.
- [6] Hirata K, Kawakami M, O'Rourke M. Pulse wave analysis and pulse wave velocity: a review of blood pressure interpretation 100 years after Korotkov. *Circulation Journal: Official Journal of the Japanese Circulation Society* 2006;70:1231–9.
- [7] Wang YX, Halks-Miller M, Vergona R, Sullivan ME, Fitch R, Mallari C, et al. Increased aortic stiffness assessed by pulse wave velocity in apolipoprotein e-deficient mice. *AJP – Heart and Circulatory Physiology* 2000;278:428–34.
- [8] Vlachopoulos C, Aznaouridis K, Stefanadis C. Prediction of cardiovascular events and all-cause mortality with arterial stiffness: a systematic review and meta-analysis. *Journal of the American College of Cardiology* 2010;55(13):1318–27.
- [9] Ibrahim ES, Johnson K, Miller A, Shaffer J, White R. Measuring aortic pulse wave velocity using high-field cardiovascular magnetic resonance: comparison of techniques. *Journal of Cardiovascular Magnetic Resonance* 2010;12(1):26–26.
- [10] Gatehouse PD, Keegan J, Crowe LA, Masood S, Mohiaddin RH, Kreitner KF, et al. Applications of phase-contrast flow and velocity imaging in cardiovascular MRI. *European Radiology* 2005;15(10):2172–84.
- [11] Horváth I, Németh A, Lenkey Z, Alessandri N, Tufano F, Kis P, et al. Invasive validation of a new oscillometric device (arteriograph) for measuring augmentation index, central blood pressure and aortic pulse wave velocity. *Journal of Hypertension* 2010;28(10):2068–75.
- [12] Boese J, Bock M, Schoenberg S, Schad L. Estimation of aortic compliance using magnetic resonance pulse wave velocity measurement. *Physics in Medicine and Biology* 2000;45(6):1703–13.
- [13] Vulliémoz S, Stergiopoulos N, Meuli R. Estimation of local aortic elastic properties with MRI. *Magnetic Resonance in Medicine* 2002;47(4):649–54.
- [14] Giri S, Ding Y, Nishijima Y, Pedraza-Toscano A, Burns P, Hamlin R, et al. Automated and accurate measurement of aortic pulse wave velocity using magnetic resonance imaging. In: Computers in cardiology, 2007. 2007. p. 661–4.
- [15] Fielden SW, Fornwalt BK, Jerosch-Herold M, Eisner RL, Stillman AE, Oshinski JN. A new method for the determination of aortic pulse wave velocity using cross-correlation on 2D PCMR velocity data. *Journal of Magnetic Resonance Imaging* 2008;27(6):1382–7.
- [16] Markl M, Wallis W, Brendecke S, Simon J, Frydrychowicz A, Harloff A. Estimation of global aortic pulse wave velocity by flow-sensitive 4D MRI. *Magnetic Resonance in Medicine* 2010;63(6):1575–82.
- [17] Yu HY, Peng HH, Wang JL, Wen CY, Tseng WYI. Quantification of the pulse wave velocity of the descending aorta using axial velocity profiles from phase-contrast magnetic resonance imaging. *Magnetic Resonance in Medicine* 2006;56(4):876–83.
- [18] Herment A, Kachenoura N, Lefort M, Bensalah M, Dogui A, Frouin F, et al. Automated segmentation of the aorta from phase contrast MR images: validation against expert tracing in healthy volunteers and in patients with a dilated aorta. *Journal of Magnetic Resonance Imaging* 2010;31(4):881–8.
- [19] Kirbas C, Quek FKH. A review of vessel extraction techniques and algorithms. *ACM Computing Surveys* 2004;36:81–121.
- [20] Lesage D, Angelini ED, Bloch I, Funck-Lea G. A review of 3d vessel lumen segmentation techniques: models, features and extraction schemes. *Medical Image Analysis* 2009;13(6):819–45.
- [21] Zhao F, Zhang H, Wahle A, Thomas MT, Stolpen AH, Scholz TD, et al. Congenital aortic disease: 4D magnetic resonance segmentation and quantitative analysis. *Medical Image Analysis* 2009;13(3):483–483.

- [22] Vitanovski D, Ralovich K, Ionasec R, Zheng Y, Suehling M, Krawtschuk W, et al. Personalized learning-based segmentation of thoracic aorta and main branches for diagnosis and treatment planning. In: 2012 9th IEEE international symposium on biomedical imaging (ISBI). IEEE; 2012. p. 836–9.
- [23] Tek H, Ayvacı A, Comaniciu D. Multi-scale vessel boundary detection. In: Computer vision for biomedical image applications. Springer; 2005. p. 388–98.
- [24] Ladak HM, Thomas JB, Mitchell JR, Rutt BK, Steinman DA. A semi-automatic technique for measurement of arterial wall from black blood MRI. *Medical Physics* 2001;28:1098–107.
- [25] Rueckert D, Burger P, Forbat S, Mohiaddin R, Yang GZ. Automatic tracking of the aorta in cardiovascular MR images using deformable models. *IEEE Transactions on Medical Imaging* 1997;16(5):581–90.
- [26] Babin D, Vansteenkiste E, Pižurica A, Philips W. Segmentation and length measurement of the abdominal blood vessels in 3-D MRI images. In: Proceedings of the annual international conference of the IEEE Engineering in Medicine and Biology Society EMBC 2009. 2009. p. 4399–402.
- [27] Wang C, Frimmel H, Smedby Ö. Level-set based vessel segmentation accelerated with periodic monotonic speed function. In: SPIE medical imaging. 2011. p. 79621M.
- [28] Yushkevich PA, Piven J, Cody Hazlett H, Gimpel Smith R, Ho S, Gee JC, et al. User-guided 3D active contour segmentation of anatomical structures: significantly improved efficiency and reliability. *Neuroimage* 2006;31(3):1116–28.
- [29] Caselles V, Kimmel R, Sapiro G. Geodesic active contours. In: Proceeding conference of the fifth international computer vision. 1995. p. 694–9.
- [30] Zhu SC, Yuille A. Region competition: unifying snakes, region growing, and Bayes/MDL for multiband image segmentation. *IEEE Transactions on Pattern Analysis and Machine Intelligence* 1996;18(9):884–900.
- [31] Gao Y, Kikinis R, Bouix S, Shenton M, Tannenbaum A. A 3D interactive multi-object segmentation tool using local robust statistics driven active contours. *Medical Image Analysis* 2012;16:1216–27.
- [32] Babin D, Pižurica A, Philips W. Robust segmentation methods for aortic pulse wave velocity measurement. In: IEEE EMBS Benelux Chapter, annual symposium, abstracts (2011). 2011.
- [33] Babin D, Pižurica A, Bellens R, De Bock J, Shang Y, Goossens B, et al. Generalized pixel profiling and comparative segmentation with application to arteriovenous malformation segmentation. *Medical Image Analysis* 2012;16(5):991–1002.
- [34] Babin D, Vansteenkiste E, Pižurica A, Philips W. Segmentation of brain blood vessels using projections in 3-D CT angiography images. In: 2011 33rd annual international conference of the IEEE Engineering in Medicine and Biology Society, IEEE. 2011. p. 475–8478. ISBN 9781424441211.
- [35] van der Geest RJ, Niezen RA, van der Wall EE, de Roos A, Reiber JHC. Automated measurement of volume flow in the ascending aorta using MR velocity maps: evaluation of inter- and intraobserver variability in healthy volunteers. *Journal of Computer Assisted Tomography* 1998;22(6):904–11.
- [36] Grotenhuis HB, Westenberg JJ, Steendijk P, van der Geest RJ, Ottenkamp J, Bax JJ, et al. Validation and reproducibility of aortic pulse wave velocity as assessed with velocity-encoded MRI. *Journal of Magnetic Resonance Imaging* 2009;30(3):521–6.
- [37] Westenberg JJ, de Roos A, Grotenhuis HB, Steendijk P, Hendriksen D, van den Boogaard PJ, et al. Improved aortic pulse wave velocity assessment from multi-slice two-directional in-plane velocity-encoded magnetic resonance imaging. *Journal of Magnetic Resonance Imaging* 2010;32(5):1086–94.
- [38] Dijkstra EW. A note on two problems in connection with graphs. *Numerische Mathematik* 1959;1:269–71.
- [39] Westenberg JJM, Wasser MNJM, van der Geest RJ, Pattynama PMT, de Roos A, Vanderschoot J, et al. Variations in blood flow waveforms in stenotic renal arteries by 2D phase-contrast cine MRI. *Journal of Magnetic Resonance Imaging* 1998;8(3):590–7.
- [40] Dogui A, Redheuil A, Lefort M, DeCesare A, Kachenoura N, Herment A, et al. Measurement of aortic arch pulse wave velocity in cardiovascular MR: comparison of transit time estimators and description of a new approach. *Journal of Magnetic Resonance Imaging* 2011;33(6):1321–9.
- [41] Dice LR. Measures of the amount of ecologic association between species. *Ecology* 1945;26(3):297–302.
- [42] Mattace-Raso FU, Hofman A, Verwoert GC, Witteman JC, Wilkinson I, Cockcroft J, et al. Determinants of pulse wave velocity in healthy people and in the presence of cardiovascular risk factors: establishing normal and reference values. *European Heart Journal* 2010;31(19):2338–50.
- [43] Stevanov M, Baruthio J, Gounot D, Grucker D. In vitro validation of MR measurements of arterial pulse-wave velocity in the presence of reflected waves. *Journal of Magnetic Resonance Imaging* 2001;14(2):120–7.

Danilo Babin was born in Senta, Serbia on April 25, 1982. He received his Master of Science Degree in Telecommunications (Electrical Engineering) from the University of Novi Sad (Serbia) in 2007 and the PhD Degree in Computer Science Engineering from Ghent University (Belgium) in 2013. Since May 2008, he has been conducting research at the department of Telecommunications and Information Processing, Faculty of Engineering and Architecture, Ghent University. His research interests include image analysis, medical image segmentation, skeletonization and visualization.

Daniel Devos is a radiologist at the Radiology department of Ghent University Hospital (UZ Ghent) since 2000. His research interests include cardiovascular examinations performed with Computer Tomography and Magnetic Resonance, comprising a broad range of pathologies: congenital heart disease, cardiomyopathies, inflammatory diseases, syndromal and cardiogenetic entities, preprocedural workup for invasive arrhythmia therapy, peripheral artery disease.

Aleksandra Pižurica received the Diploma Degree in Electrical Engineering from the University of Novi Sad (Serbia) in 1994, Master of Science Degree in Telecommunications from The University of Belgrade (Serbia) in 1997 and the PhD Degree in Engineering from Ghent University (Belgium) in 2002. Since 2005 she is a post-doctoral research fellow of The Research Foundation – Flanders (FWO) and since 2009 she is also as a part time lecturer at Ghent University. Her research interests include statistical image modeling, multiresolution and sparse signal representations, Bayesian estimation and applications in video analysis, remote sensing and medical imaging.

Jos Westenberg is an assistant professor at the Department of Radiology, LUMC, Utrecht area, the Netherlands since 2010. He has more than 70 published articles in international peer-reviewed scientific journals. His research expertise and interests include MRI, medical imaging and image analysis.

Ewout Vansteenkiste was born in Kortrijk, Belgium (03/05/1978). He obtained a MSc in Pure Mathematics for Ghent University in 2000, and a PhD in engineering at the same university in 2007, focusing on medical image processing. He is currently working as a valorisation manager for a consortium of Ghent university research groups focusing on hybrid computed tomography and its applications.

Wilfried Philips was born in Aalst, Belgium on October 19, 1966. In 1989, he received the Diploma degree in electrical engineering and in 1993 the Ph.D. degree in applied sciences, both from Ghent University, Belgium. From October 1989 until October 1997 he worked at the Department of Electronics and Information Systems of Ghent University as a research assistant and later as a post-doctoral research fellow. Since November 1997 he is with the Department of Telecommunications and Information Processing of Ghent University, where he is currently a full-time professor and is heading the research group “Image Processing and Interpretation”.